

See discussions, stats, and author profiles for this publication at: <https://www.researchgate.net/publication/23386550>

# Topological Analysis of the Reaction of Uranium Ions ( $U^+$ , $U^{2+}$ ) with $N_2O$ in the Gas Phase

ARTICLE in THE JOURNAL OF PHYSICAL CHEMISTRY A · NOVEMBER 2008

Impact Factor: 2.69 · DOI: 10.1021/jp803269j · Source: PubMed

---

CITATIONS

29

---

READS

43

## 4 AUTHORS, INCLUDING:



M. Esmail Alikhani

Pierre and Marie Curie University - Paris 6

107 PUBLICATIONS 1,264 CITATIONS

SEE PROFILE



Nino Russo

Università della Calabria

512 PUBLICATIONS 7,933 CITATIONS

SEE PROFILE

# Topological Analysis of the Reaction of Uranium Ions ( $U^+$ , $U^{2+}$ ) with $N_2O$ in the Gas Phase<sup>†</sup>

Mohammad Esmail Alikhani,<sup>‡</sup> Maria del Carmen Michelini,<sup>§</sup> Nino Russo,<sup>\*,§</sup> and Bernard Silvi<sup>\*,||</sup>

Laboratoire de Dynamique, Interactions et Réactivité (UMR 7075), Université P. et M. Curie, Paris Cedex 05, France, Dipartimento di Chimica and Centro di Calcolo ad Alte Prestazioni per Elaborazioni Parallele e Distribuite-Centro d' Eccellenza MURST, Università della Calabria, Arcavacata di Rende, Italy, and Laboratoire de Chimie Théorique (UMR 7616), Université P. et M. Curie, Paris Cedex 05, France

Received: April 15, 2008; Revised Manuscript Received: July 16, 2008

Density functional theory calculations were performed to study the ability of uranium cations,  $U^+$  and  $U^{2+}$ , to activate the N–N and N–O bonds of  $N_2O$ . A close description of the reaction pathways leading to different reaction products is presented. The obtained results are compared with previous experimental works. The nature of the bonding of all the involved species and the bonding evolution along the reaction pathways was studied by means of the topological analysis of the ELF function.

## 1. Introduction

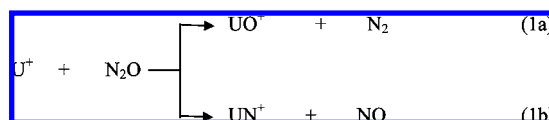
During the last decades a great body of studies has been performed on the reactivity of actinide cations with small molecules in the gas phase. This research has been mainly carried out using mass spectroscopic techniques, which are able to provide thermochemical data as well as some insight into the reaction mechanisms.<sup>1–7</sup> Some recent reviews on the subject demonstrate the increasing interest in this area.<sup>1,2</sup> The main goal of this kind of research has been to analyze the reactivity and bonding of the metal ions, which in the absence of perturbing factors correlate directly with their electronic structures and energetics. In the case of early actinides it is particularly interesting to analyze the possible active role of the 5f electrons in reactivity.

Some recent theoretical calculations have permitted us to get a detailed description of the reaction mechanisms of activation of small molecules by bare actinide cations.<sup>8–10</sup> It has been shown that, as in the case of reactions involving first- and second-row transition metal cations, they usually involve more than one spin state. This kind of behavior, in which more than one spin surface connects reactants and products, is generally referred to as two-state reactivity (TSR)<sup>11</sup> and is known to play a fundamental role in reactions involving transition metals.<sup>12</sup> In addition, in the case of actinide chemistry the formal spin may vary during a reaction without appreciably affect the rate due to the fact that weak spin–orbit coupling (Russell–Saunders coupling) does not apply to the heavy metal ions. Instead, strong spin–orbit coupling (jj-coupling) better describes the electronic states and the requirement for spin conservation is thereby relaxed. Recent theoretical works involving gas phase reactions of bare uranium atom and cations with small molecules have shown the importance of taking into account different spin states.<sup>8–10,13,14</sup> In addition, for the reactions studied here, it must also be taken into account that singlet  $N_2O$  decomposes to singlet

$N_2$  and triplet O, which is a spin-forbidden process. Bohme and collaborators have recently performed a comprehensive study of the reactivity of first-, second- and third-row atomic monocations with  $N_2O$ ,<sup>15</sup> in addition to an earlier study of the reactivity of lanthanide cations and  $N_2O$ .<sup>16</sup> The reactivity of first- and second-row transition metal cations and  $N_2O$  has also been theoretically studied,<sup>15,17</sup> whereas to the best of our knowledge this is the first theoretical study of the reaction mechanisms of actinide cations with  $N_2O$ .

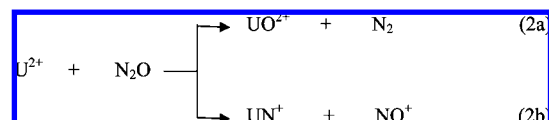
Early studies of the reactivity of  $U^+$  and  $U^{2+}$  with nitrous oxide have been performed by Schwarz and collaborators using Fourier transform ion cyclotron resonance mass spectrometry (FTICR-MS).<sup>3,4</sup> More recently, the reactivity of mono- and dipositive actinide ions with several oxidants was systematically investigated by Gibson and co-workers.<sup>1,2,5,6</sup>

In the case of the reaction between  $U^+$  and  $N_2O$  the following reaction products were experimentally detected (FTICR-MS)<sup>4,5</sup>



The monocationic uranium oxide is the primary reaction product, with a branching ratio of 60%<sup>5</sup> (70% according to the earlier studies).<sup>4</sup>

In the case of the reaction between the double charged cation and nitrous oxide,  $UO^{2+}$  and  $UN^+$  were the reaction products observed in FTICR-MS experiments:



For this reaction the product distribution indicates a substantial fraction of  $UN^+$ , with a branching ratio of 45%<sup>7</sup> (20% according to earlier studies<sup>3</sup>).

<sup>†</sup> Part of the "Sason S. Shaik Festschrift".

\* Authors to whom correspondence should be addressed. E-mail: N.R., nrusso@unical.it; B.S., silvi@lct.jussieu.fr.

<sup>‡</sup> Laboratoire de Dynamique, Interactions et Réactivité (UMR 7075), Université P. et M. Curie.

<sup>§</sup> Università della Calabria.

<sup>||</sup> Laboratoire de Chimie Théorique (UMR 7616), Université P. et M. Curie.

The measured reaction efficiencies indicate that both reactions are quite efficient ( $k/k_{COL} = 0.47$  for  $U^+ + N_2O^5$  and  $0.40$  for  $U^{2+} + N_2O^7$ ).

The main goal of this work is to perform a detailed study of the gas phase reaction mechanisms of the interaction of  $U^+$  and  $U^{2+}$  with  $N_2O$ , with a special interest into the analysis of the topological features of all the involved species and the description of the bonding evolution during the reaction pathways.

## 2. Computational Details

The density functional theory in its three-parameter hybrid B3LYP formulation<sup>18</sup> was the computational method used for geometry optimizations and frequency calculations together with the Stuttgart basis sets<sup>19</sup> for the uranium atom, (25s 16p 15d 7f)/[7s 6p 5d 3f] in combination with the small-core relativistic effective core potential (RECP). The small-core RECP replaces the 60 electrons in inner shells 1–4 leaving the explicit treatment of the  $n = 5$  shell (5s, 5p, 5d, and 5f) and also the 6s, 6p, 6d and 7s valence electrons. The 6-311++G(2d,2p) basis set of Pople and co-workers<sup>20</sup> was employed for the rest of the atoms. The calculations were carried out with GAUSSIAN03 package.<sup>21</sup> The singlet state optimizations were done within the restricted Kohn–Sham formalism, whereas the open-shell structures were studied using the unrestricted approach. For the reaction pathway analysis we have ensured that every transition structure has only one imaginary frequency, and that it connects the reactants to the appropriate products by means of IRC (Intrinsic Reaction Coordinate) calculations. For all the studied species we have checked the  $\langle S^2 \rangle$  values to evaluate whether spin contamination can influence the quality of the results. Only in some of the doublet spin species we have found that the obtained values differ from  $S(S + 1)$  by between 5 and 10%. The rest of the structures do not present spin contamination problems.

The TopMod package<sup>22</sup> was used to analyze the chemical bonding of the studied species from a topological point of view and the results were visualized with the help of the Molekel 4.0<sup>23</sup> and Amira 3.1<sup>24</sup> softwares. The topological description of the chemical bond proposed by Silvi and Savin<sup>25</sup> is based on the gradient field analysis of the electron localization function (ELF) of Becke and Edgecombe.<sup>26</sup> ELF is a scalar function whose gradient field enables us to carry out a partition of the molecular space into basins of attractors closely related to Gillespie's electronic domains. As mentioned by Gillespie and Robinson,<sup>27</sup> "The electron localization function exhibits maxima at the most probable positions of localized electron pairs and each maximum is surrounded by a basin in which there is an increased probability of finding an electron pair. These basins correspond to the qualitative electron pair domains of the VSEPR model and have the same geometry as the VSEPR domains." The valence shell of a molecule consists of two types of basin: polysynaptic basins (generally disynaptic), which belong to two atomic valence shells and the monosynaptic ones, which belong to only one valence shell, and which qualitatively correspond to nonbonding valence density. The valence basins are labeled by V followed by a list of the atomic symbols of the centers of the valence shells, i.e.,  $V(A)$  and  $V(A,B)$  for a monosynaptic and a disynaptic basin. The basin populations and the associated covariance matrix are calculated by integration of the one electron and pair densities over the volume of the basins enabling a phenomenological interpretation of the population analysis in terms of the superposition of mesomeric structures.<sup>28</sup> This analysis has provided very useful pieces of information on the bonding for a wide range of chemical cases.<sup>29</sup>

To analyze the evolution of the bonding during the reaction we have used the so-called bonding evolution theory (BET).<sup>30</sup>

This theory is based on a joint use of the ELF approach and the catastrophe theory<sup>31</sup> to identify changes between regions of structural stability in processes of forming/breaking of chemical bonds along the reaction path. This approach has been applied to characterize different chemical processes.<sup>32</sup>

## 3. Results

For the reaction of  $U^+ + N_2O$  we have studied three different spin states: quartet, sextet and doublet. The ground state (GS) of the bare  $U^+$  is a  $^4I_{9/2}$  derived from the  $[Rn]5f^37s^2$  configuration.<sup>33</sup> The three lowest-energy excited states are  $^6L_{11/2}$  ( $[Rn] 5f^3 6d 7s$ ) at 0.83 kcal/mol,  $^6M_{13/2}$  ( $[Rn] 5f^3 6d^2$ ) at 13.11 kcal/mol, and  $^6I_{7/2}$  ( $[Rn] 5f^47s$ ) at 13.33 kcal/mol. The first doublet spin state,  $^2I_{9/2}$  ( $[Rn] 5f^37s^2$ ), is at 21.71 kcal/mol over the  $^4I_{9/2}$  ground state.<sup>33</sup> In previous works we have checked the reliability of the employed level of theory,<sup>8–10</sup> and we have calculated the energy gaps for both cations ( $U^+$  and  $U^{2+}$ ) using different DFT approximations.<sup>8</sup> At the B3LYP/SDD level the quartet spin GS is followed by two sextet states with  $[Rn] 5f^36d^17s^1$  and  $[Rn] 5f^47s^1$  electronic configurations, at 1.5 and 4.1 kcal/mol higher in energy, respectively. The  $[Rn] 5f^37s^2$  doublet spin state was found to be around 18.2 kcal/mol over the quartet ground state.

In the case of  $U^{2+}$ , we have studied quintet, triplet and singlet spin states. The GS of the bare dication is a  $^5I_4$  derived from the  $[Rn]5f^4$  configuration whereas the lowest-energy triplet spin state,  $^3H_4$  ( $[Rn]5f^27s^2$ ), is about 105 ( $\pm 17$ ) kcal/mol higher in energy.<sup>33</sup> At B3LYP/SDD level we correctly identify the  $[Rn]5f^4$  quintet GS configuration, whereas the  $[Rn]5f^4$  and  $[Rn]5f^27s^2$  triplet states were found at +36.9 kcal/mol and +100.1 kcal/mol, respectively. For more details regarding the comparison of the relative energies of the bare uranium cations, see ref 8.

**3.1.  $U^+ + N_2O$  Reaction.** We have analyzed different coordination modes between the metal cation and  $N_2O$ : the "side-on" approach with respect to the N–O and N–N bonds, and the "end-on" one, in which the cation interacts with the (O,N) ending atoms of nitrous oxide, with a nearly linear arrangement. Each geometrical structure was investigated for the three studied spin states. According to our calculations, the only reaction pathway that leads to the formation of  $UO^+ + N_2$ , reaction channel **1a**, starts with the N-end coordination mode. The initial step involves the exothermic formation of an association complex,  $U^+ - NNO$ . Then, the system passes through a transition state, **TS<sub>1a</sub>**, which contains the O and U atoms in a cis position with respect to the N–N bond that allows the transfer of the terminal O atom to the metal cation leading to the formation of the  $OU^+ - N_2$  insertion intermediate. That intermediate is a deep minimum (–145.0 kcal/mol) of the potential energy profile (PEP) and has a quite long U–N bond length (2.637 Å). Owing to the large internal energy and the geometrical features of the  $OU^+ - N_2$  intermediate, the  $N_2$  elimination can be easily envisaged. The overall PEP for the reaction **1a** is sketched in Figure 1a. In that figure we report the relative energies of all of the species involved in the quartet, sextet and doublet spin pathways, with respect to the  $U^+ + N_2O$  reactants GS. The quartet spin state remains as the ground state for the whole reaction path **1a**. The sextet state is very close to the quartet at the entrance channel but becomes high in energy just after the surpassing of the transition state. Therefore, for the channel **1a** we will restrict our discussion to the quartet ground spin state. The geometrical parameters of all of the minima and transition states involved in the reaction channel **1a** are shown in Figure 2a. We note that the transition state, **TS<sub>1a</sub>** ( $i$  151  $cm^{-1}$ ) that has an intrinsic barrier height of almost 6 kcal/mol, is

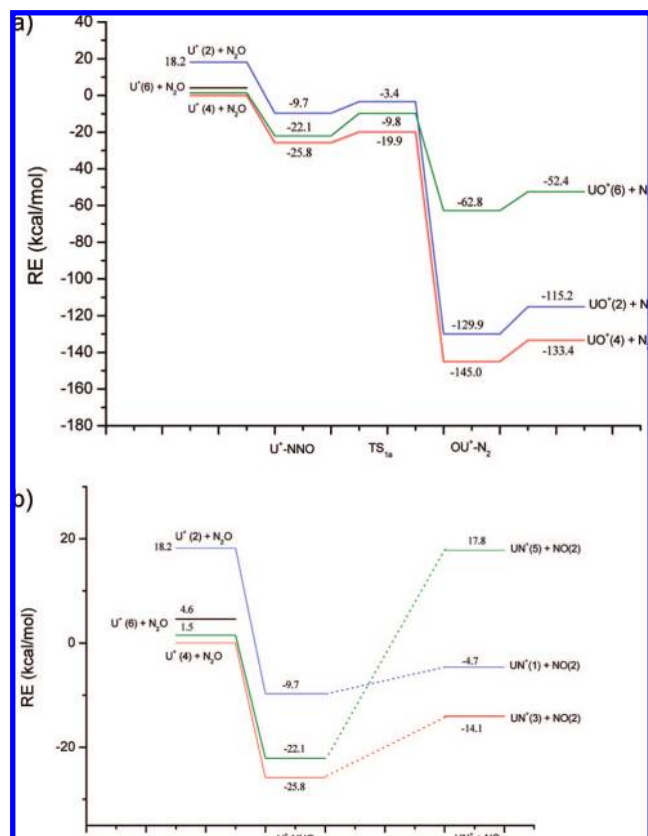


**Figure 1.** Schematic representation of the B3LYP/SDD potential energy profiles corresponding to (a) reaction channel **1a** and (b) reaction channel **1b**. Spin multiplicities are given in parenthesis.

energetically well below the asymptote represented by the reactants. The calculated exothermicity of the whole process (reaction **1a**) is of almost 134 kcal/mol (Figure 1a). This result is in good agreement with the  $-145 (\pm 5)$  kcal/mol calculated from estimations based on the experimental U–O<sup>+</sup> and N<sub>2</sub>–O bond dissociation energies.<sup>2,34</sup> As previously mentioned, we have analyzed different ligand interactions modes, and we have found that the formation of the O-end complex U<sup>+</sup>–ONN is less favored (the process is exothermic by around 12.9 kcal/mol compared to the 25.8 kcal/mol of the N-end adduct formation) and does not evolve to the elimination of N<sub>2</sub>. The U<sup>+</sup>–ONN complex in the lowest-energy quartet state is characterized by a U–O bond length of 2.49 Å, an ∠UON angle of 159.5°, and the N<sub>2</sub>O moiety is almost perfectly linear.

The reaction of U<sup>+</sup> and N<sub>2</sub>O to activate the N–N bond, reaction channel **1b**, shares with the previously described reaction, the U<sup>+</sup>–NNO initial complex. From this structure, the formation of UN<sup>+</sup> (<sup>3</sup>Σ<sub>g</sub>) + NO is an endothermic process, as shown in Figure 1b. The computed exothermicity of reaction **1b** is of around 14 kcal/mol. We note that, in contrast to the previously studied reaction, the initial complex separates in two fragments, both of which have total spin different to zero. The geometrical parameters of all the structures involved in the channel **1b** are collected in Figure 2.

**3.1.1. Bonding Analysis.** To have a deeper understanding of the reaction mechanisms, we have first analyzed the bonding of each of the species involved in the reaction pathways, at all the studied spin states, using the topological analysis of the ELF function.

The ELF calculation fails to provide a clear core-valence separation on the uranium center. As can be seen in Figures 2 and 6, there is a rather large number of small basins around the

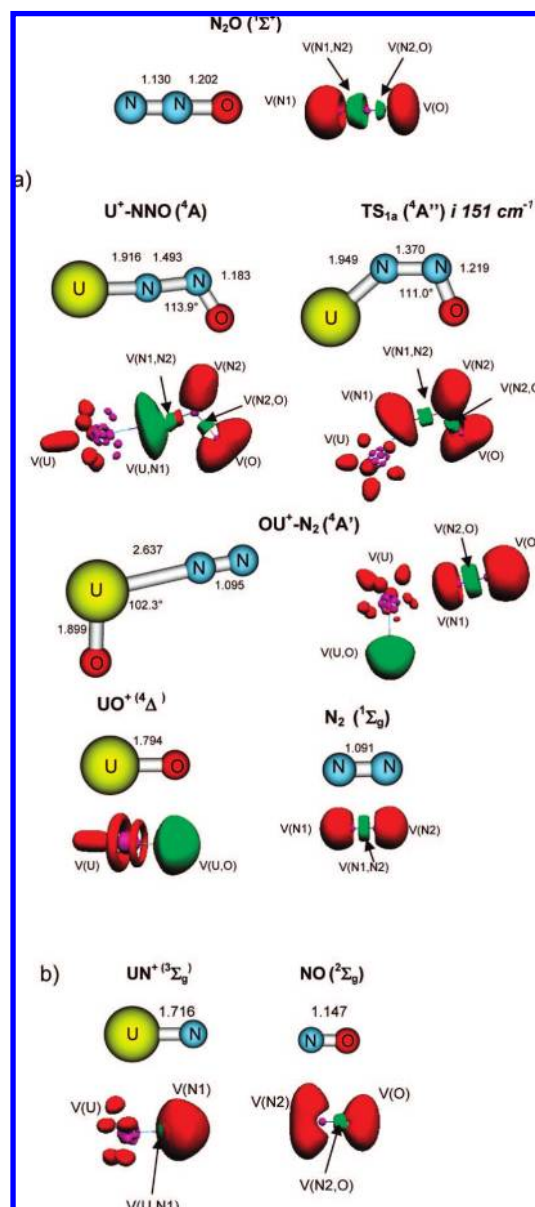


**Figure 2.** Geometrical parameters and ELF localization domains ( $\eta = 0.75$ ) of the lowest-energy minima and transition states corresponding to (a) reaction channel **1a** and (b) reaction channel **1b**. Bond lengths are in angstrom and angles in degrees.

uranium core assigned to monosynaptic valence basins by TopMoD; however, the sums of the population of these basins are noticeably over the expected values whereas the total basin population of C(U) + V(U) is always less than 30.1 e. Therefore, these basins belong to the external core shell in which the node structure of the 4f, 6d and 5f pseudo-orbitals is probably responsible for these complicated patterns. The localization domains corresponding to the lowest-energy minima and transition states of pathways 1a and 1b are shown in Figure 2, whereas the corresponding basin populations are reported in Table 1. As can be seen in Figure 2 and Table 1, the formation of the first complex in the lowest-energy quartet spin state provokes important topological changes in the ligand. The U<sup>+</sup>–NNO (<sup>4</sup>A) complex is characterized by the presence of a disynaptic valence basin between the terminal N and the U atom, V(U,N1), with an electron population of 5.54 electrons. The contribution to that population coming from the metal atom is very low, namely, around 8%. The folding of the N<sub>2</sub>O moiety



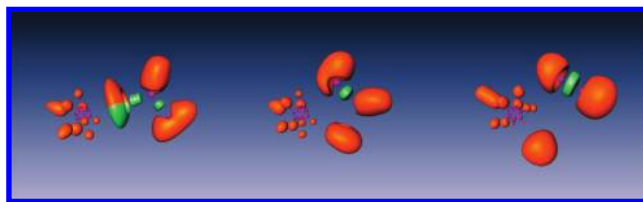
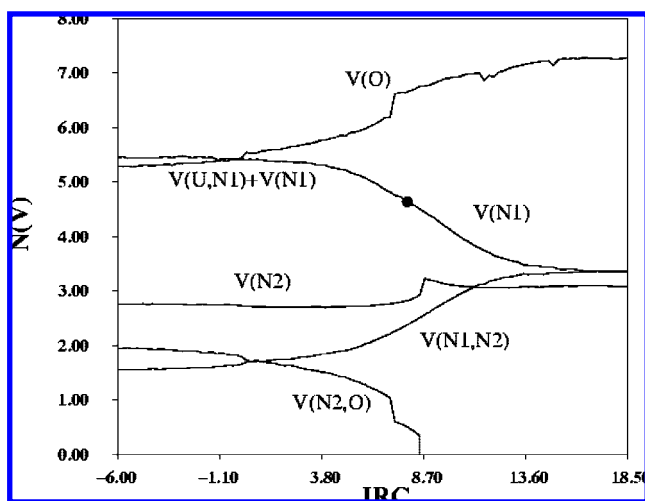
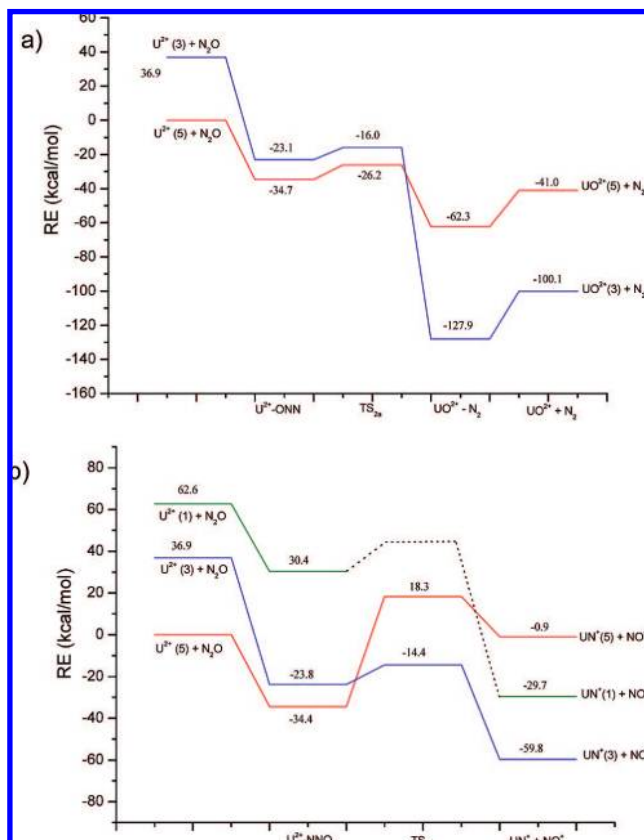
**TABLE 1: Basin Population,  $\bar{N}$ , and Integrated Spin Densities,  $\langle S_z \rangle$ , of the Key Minima Found along the  $U^+ + N_2O$  Reaction Channels 1a and 1b**

basin	$N_2O$ ( $^1\Sigma_g$ )	$U^+-NNO$ ( $^4A$ )		$TS_{1a}$ ( $^4A''$ )		$OU^+-N_2$ ( $^4A'$ )		$UO^+$ ( $^4\Delta$ )		$N_2$ ( $^1\Sigma_g$ )	$UN^+$ ( $^3\Sigma_g$ )		$NO$ ( $^2\Sigma_g$ )	
	$\bar{N}$	$\bar{N}$	$\langle S_z \rangle$	$\bar{N}$	$\langle S_z \rangle$	$\bar{N}$	$\langle S_z \rangle$	$\bar{N}$	$\langle S_z \rangle$	$\bar{N}$	$\bar{N}$	$\langle S_z \rangle$	$\bar{N}$	$\langle S_z \rangle$
C(U)+V(U)		29.61	1.51	29.66	1.53	29.56	1.38	29.41	1.50		29.63	1.07		
V(O)	6.04	5.24		5.45									4.88	0.16
V(N1)	4.06					3.15				3.21	6.24	-0.06	1.92	0.15
V(N2)		2.76		2.72		3.35	0.02			3.21			1.92	0.15
V(U,O)						7.24	-0.02	7.44						
V(U,N1)		5.54		5.41	-0.02						0.91	0.01		
V(N1,N2)	3.48	1.54		1.66		3.37				3.38				
V(N2,O)	2.01	1.97		1.79									2.04	

and the activation of the N–O bond are characterized by the appearance of a monosynaptic valence basin on the central N atom, V(N), which has an electron population of 2.76 electrons. It has been previously reported<sup>35</sup> that the  $N_2O^-$  anion shows a monosynaptic basin in the central nitrogen atom, and the formation of that basin gives an explanation to the NNO bond angle and the lengthening of the bonds. The N–N bond is already quite weakened in the initial complex, as demonstrated by the important lowering of the V(N1,N2) electron population after the adduct formation (Table 1). The formation of the  $TS_{1a}$  transition state involves only small variations of the valence basin populations, all of which are in line with the small changes of the bond lengths. The formation of the insertion intermediate involves the broken of the U–N1 bond, as evidenced by the disappearance of the corresponding disynaptic basin. The presence of the V(U,O) disynaptic valence basin with an electron population (7.24 e) very close to that of the free  $UO^+(^4\Delta)$  basin (7.44 e), indicates that this structure can be described as formed from two fragments,  $UO^+$  and  $N_2$ . The populations of the basins associated with the  $N_2$  moiety are also very close to that of the free  $N_2$  molecule (Table 1). The  $UO^+(^4\Delta)$  is characterized by the presence of a disynaptic V(U,O) basin with a total population of 7.44 e. The contribution of the metal atom to that population is close to 10%. In all the structures involved in the reaction pathways the spin density is always located on the metal center (see  $\langle S_z \rangle$  values in Table 1).

**3.1.2. Reaction 1a Mechanism.** To investigate the electronic mechanism of reaction 1a, 104 single point calculations have been carried out along the reaction path. An animation of the

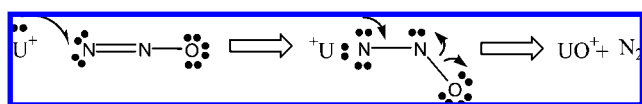
reaction is provided by the reac1a.mpeg file available in the Supporting Information. Figure 3 displays the evolution of the valence basin populations of the  $N_2O$  moiety along the reaction path on both sides of  $TS_{1a}$  ( $^4A''$ ). The formation of the initial complex is characterized by a transfer of about 1 e from  $U^+$  toward  $N_2O$ , this electron density is not polarized because the unpaired electrons remain on the U side. It increases the population of the V(N1) basin of the isolated  $N_2O$ , which

**Figure 4.** Snapshots of the ELF localization basins for the reaction coordinates (arbitrary units) from left to right  $R = -6.0, 8.7$  and  $18.5$ , of the reaction pathway 1a.**Figure 3.** Evolution of the basin populations of the  $N_2O$  moiety along the IRC (arbitrary units) for reaction 1a. The black dot of the V(U,N1)+V(N1)/V(N1) curve localizes the change of synaptic order of the V(U,N1) basin.**Figure 5.** Schematic representation of the B3LYP/SDD potential energy profiles corresponding to the reaction channels 2a and 2b, respectively. Spin multiplicities are given in parenthesis.

**TABLE 2: Basin Population,  $\bar{N}$ , and Integrated Spin Densities,  $\langle S_Z \rangle$ , of the Key Minima Found along the  $U^{2+} + N_2O$  Reaction 2a**

basin	$N_2O (^1\Sigma_g)$	$U^{2+}-ONN (^5A'')$		$TS_{2a} (^5A'')$		$UO^{2+}-N_2 (^3A'')$		$UO^{2+} (^3\Sigma_g)$		$N_2 (^1\Sigma_g)$
	$\bar{N}$	$\bar{N}$	$\langle S_Z \rangle$	$\bar{N}$	$\langle S_Z \rangle$	$\bar{N}$	$\langle S_Z \rangle$	$\bar{N}$	$\langle S_Z \rangle$	$\bar{N}$
C(U) + V(U)		30.09	1.98	29.84	1.83	28.63	0.95	28.69	1.04	
V(O)	6.04	5.90	0.01	6.22	0.03					
V(N1)				1.97	0.05	3.29				3.21
V(N2)	4.06	3.36		3.32		3.00				3.21
V(U,O)						7.30	-0.04	7.15	-0.04	
V(N1,N2)	3.48	4.75		3.39	0.01	3.45				3.38
V(N1,O)	2.01	1.59		0.93						

becomes disynaptic with the formation of a U–N dative bond. Another charge transfer occurs from the V(N1,N2) basin, which leads to the formation of V(N2); thus the electronic environment around the N2 center is of the AX2E VSEPR type, which explains the bent structure of the complex. Moreover, in the complex the V(N1,N2) basin is in fact split into two monosynaptic basins V(N1) and V(N2) such as for in the case of electron density depleted or protocovalent bonds.<sup>36</sup> Figure 4 shows three typical bonding situations taken along the reaction path taken before and after the transition state. As the transition state and the complex are close in energy, there is no important change in the ELF topology of these structures, in agreement with the Hammond's postulate. However, the N–N bond is no longer protocovalent because the V(N1) and V(N2) basins have been reunified by a cusp catastrophe.<sup>30</sup> The population of V(N1,N2) has increased at the expense of V(U,N1) and of V(N2) and consequently the N–N distance is shortened. Figure 4 also shows a transfer of electron density from the V(N2,O) basin to the V(O) ones until the first discontinuity of the V(N2,O) curve, which corresponds to a cusp catastrophe yielding a small V(O) basin rapidly merged to main ones by a fold catastrophe<sup>30</sup> whereas V(N2,O) collapses into V(N2) by the same process. The last part of the reaction path is driven by the UNN in-plane bending, which yields the formation of the products. A schematic representation of the mechanism in which curly arrows represent electron density transfers is



**3.1.3. Reaction 1b Mechanism.** The mechanism **1b** is much more straightforward because in the  $U^+-NNO$  complex at equilibrium, the V(N1,N2) basin is already split into two monosynaptic basins. When the N1–N2 distance becomes larger than 1.73 Å, V(N2) vanishes and the V(N1) population starts to increase. The unpaired electron density remains entirely localized on the U center for N1–N2 distances less than 2.1 Å.

**3.2.  $U^{2+} + N_2O$ .** In the case of the reaction of  $U^{2+}$  we have studied three different spin states: quintet, triplet and singlet. As in the previous reaction, we have considered different coordination modes and we have found that the lowest-energy structures of the initial adduct involve quasi-linear geometries. In contrast to the monocationic complexes, in this case the relative stability of the  $U^{2+}-ONN$  and  $U^{2+}-NNO$  adducts with respect to the reactant asymptote is very close (around -35 kcal/mol). In Figure 5 are shown the reaction pathways for the channels **2a** and **2b**. In that figure we report the relative energies of all the species with respect to the  $U^{2+} + N_2O$  ground state fragments. As can be seen in Figure 5a, the reaction channel for the activation of the O–N bond, starts with the exothermic

**TABLE 3: Basin Population,  $\bar{N}$ , and Integrated Spin Densities,  $\langle S_Z \rangle$ , of the Key Minima Found along the  $U^{2+} + N_2O$  Reaction Channel 2b**

basin	$U-NNO^{2+} (^5A')$		$TS_{2b} (^3A'')$		$UN^+ (^3\Sigma_g)$		$NO^+ (^1\Sigma_g)$
	$\bar{N}$	$\langle S_Z \rangle$	$\bar{N}$	$\langle S_Z \rangle$	$\bar{N}$	$\langle S_Z \rangle$	$\bar{N}$
C(U) + V(U)	30.06	1.97	29.73	1.54	29.63	1.07	
V(O)			2.31	0.15			3.87
V(O)	5.22		2.47	0.06			
V(N1)	4.32	0.01	0.39	0.15	6.24	-0.06	2.88
V(N1)							
V(N2)			2.63	0.08			
V(U,N1)			5.65		0.91	0.01	
V(N1,N2)	3.77						
V(N2,O)	2.27		2.26				3.04

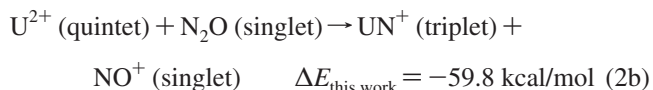
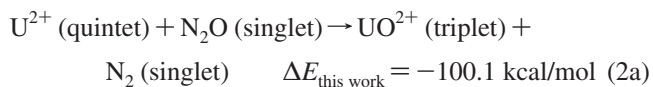
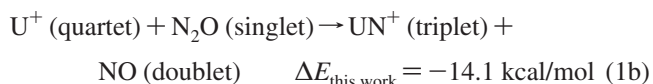
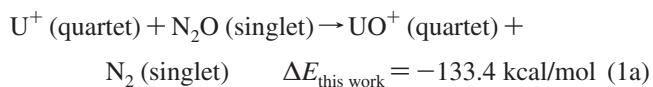
formation of the  $U^{2+}-ONN$  complex in the quintet spin state. The N–O bond length shows a slight increase upon the complex formation, whereas the N–N distance slightly decreases (see Figures 2 and 6). The formation of the  $UO^{2+} (^3\Sigma_g) + N_2$  products implies the surpassing of a transition state, **TS<sub>2a</sub>**, which has an imaginary frequency ( $i\ 1049\text{ cm}^{-1}$ ) corresponding to the N–O bond stretching. The intrinsic barrier height associated to this transition structure is of almost 8 kcal/mol. The transition state, however, is well below the  $U^{2+} + N_2O$  asymptotes limit (-26.2 kcal/mol). An intersystem crossing between the quintet and triplet spin surfaces takes place just after the system surpasses the transition structure, because the ground spin state of the  $UO^{2+}-N_2$  insertion intermediate as well as the reaction products, is the triplet. Our calculations indicate that the exothermicity of reaction channel **2a** is around 100 kcal/mol (Figure 5a). From experimental estimations of  $N_2-O$  and  $U-O^{2+}$  bond dissociation energies<sup>34,7</sup> the expected value is of around -125 ( $\pm 14$ ) kcal/mol.

We note the different reaction mechanism found for the activation of the N–O bond by  $U^+$  and  $U^{2+}$ . We must mention that we have tried to find for  $U^{2+}$  a reaction mechanism similar to that found for  $U^+$ , in which the N–O bond activation starts with the formation of the N-end complex. However, all the attempts have failed, because the formation of the  $U^{2+}-NNO$  adduct leads only to the N–N bond activation, channel **2b**, which evolves as follows. After the formation of the initial  $U^{2+}-NNO$  complex in the quintet ground state, the formation of the transition state provokes a crossing between the triplet and quintet spin surfaces. In this case, therefore, the spin crossing occurs before the system has surmounted the transition state, in contrast to the previously analyzed channel **2a**. In fact, the lowest-energy transition state, **TS<sub>2b</sub>**, which is characterized by an imaginary frequency ( $i\ 1097\text{ cm}^{-1}$ ) that corresponds to the N–N bond stretching, has the triplet ground spin state (Figures 5b and 6b). The  $U^{2+}-NNO$  cation is thermodynamically unstable with respect to the dissociation into the  $UN^+ + NO^+$  fragments, which can be understood considering that the IE of  $UN^+$  (calculated value: 323 kcal/mol) exceeds the NO IE

(calculated value: 225 kcal/mol) and the  $UN^{2+}-NO$  binding energy (calculated value: 73.1 kcal/mol) does not compensate for the difference of the IEs. However, it must be mentioned that, to drive conclusions about the kinetics of the charged products separation, the possibility of kinetic hindrance to such separation should be also taken into account. Our calculations indicate that the channel **2b** has an exothermicity of almost 60 kcal/mol with respect to the reactants asymptote. Also in this case the reaction barrier is below the reactants asymptote (−14.4 kcal/mol). We note that for the products the singlet spin surface is closer to the triplet ground state than the quintet state. This is the reason for which we have also studied the singlet state, despite the fact that the bare  $U^{2+}$  singlet state is quite high in energy (+62.6 kcal/mol at B3LYP/SDD level of theory). As can be seen in Figure 5b, we were unable to locate the transition state on the singlet spin surface, however, from the shape of the PES it can be concluded that the singlet spin state is not relevant for this reaction.

The optimized geometrical parameters of the lowest-energy spin state structures involved in the reaction channel **2a** and **2b** are displayed in Figure 6.

**3.2.1. Comparison of the Energetic Results.** As suggested by one of the referees of this article, we have checked the interconsistency of the energetical results obtained for the mono- and dicationic reactions. The computed reaction energies can be summarized as follows:



Considering the calculated energy for reaction 1a and the experimental values for  $U^+$  and  $UO^+$  ionization energies (IEs: 274.4<sup>37</sup> and 293.0<sup>7</sup> kcal/mol), we would obtain a  $\Delta E$  for reaction 2a of around 115 ( $\pm 18$ ) kcal/mol. Considering the experimental uncertainty, our results fit well the estimated value. We note, however, that the difference between the calculated and the estimated value is originated by the underestimation of the experimental  $U^+$  IE (270.7 kcal/mol at B3LYP/SDD level compared with the 274.4 kcal/mol<sup>37</sup>) and mainly from the overestimation of the  $UO^+$  IE (303.8 kcal/mol at B3LYP/SDD vs the 293.0 experimental value).<sup>7</sup>

Analogously, when combining reaction 1b with the experimental  $U^+$  and NO ionization energies (274.4 and 213.6 kcal/mol<sup>34</sup>), we can estimate the exothermicity of reaction 2b to be about −75 kcal/mol. Once again we note a difference with respect to the calculated value (−59.8 kcal/mol) of around 15 kcal/mol. Also in this case the source of the difference is the calculated ionization energies, which, as previously mentioned, in the case of  $U^+$  the experimental value is underestimated by almost 4 kcal/mol, whereas in the case of NO, is overestimated by around 12 kcal/mol (225.01 kcal/mol at B3LYP/SDD value compared to the 213.6 kcal/mol). Also in this case the errors add up, giving a difference of around 15 kcal/mol between the computed energetics of (2b) and the estimated value obtained from the experimental IEs.

**3.2.2. Bonding Analysis.** As mentioned in the previous section, channel **2a** starts with the formation of the  $U^{2+}-ONN$  complex in the quintet spin state. The localization domains corresponding to the lowest-energy minima and transition states of pathway **2a** are shown in Figure 6a. The corresponding basin populations are collected in Table 2. As can be seen, the stabilization of the initial adduct does not imply the formation of a chemical bond between the fragments ( $U^{2+}$  and  $N_2O$ ). We note that the metal–ligand distance is much larger than the value found in the monocationic case (2.364 Å vs 1.916 Å in  $U^+-NNO$ ). However, the interaction between the moieties provokes some redistribution of charge between the basins of  $N_2O$  (Table 2). In particular, the decrease of the  $V(N1,O)$  basin population (1.59 e versus the 2.01 e in the free  $N_2O$ ) is an indication of the weakening of the N–O bond that takes place after the formation of the initial ion–molecule complex. In contrast, the  $V(N1,N2)$  basin shows an important increase of the electronic population at the expense of the diminishing of the  $V(N2)$  and  $V(N1,O)$  populations. These changes are in line with the slight lengthening of the N–O distance (1.229 Å in the quintet  $U^{2+}-ONN$  complex versus 1.202 Å in the free ligand), and the slight shortening of the N–N distance (1.107 Å versus 1.130 Å in free  $N_2O$ ) that occurs after complexation. The formation of the transition state, **TS<sub>2a</sub>** in the  $^5A''$  state implies a further weakening of the N–O bond,  $V(N1,O) = 0.93$  e. We note the absence of a disynaptic valence basin between U and O in the **TS<sub>2a</sub>**. The insertion intermediate,  $UO^{2+}-N_2$ , can be considered as formed from two fragments, as demonstrated by the basin populations present in that structure (see Table 2). The reaction product,  $UO^{2+}(^3\Sigma_g^-)$  is characterized by the presence of a disynaptic  $V(U,O)$  valence basin with an electron population of 7.15 e. The contribution to that population brought by the U atom is quite low, namely around 10% of the total population. As can be seen in Table 2, the spin density is always located on the metal atom (see  $\langle S_z \rangle$  values).

**3.2.3. Reaction 2a Mechanism.** The reac2a.mpeg file available in the Supporting Information clearly shows the electronic rearrangement along the intrinsic reaction coordinate of the quintet state before the crossing point and of the triplet after. At the crossing point both energies and both reaction coordinates are equal. The evolution of the basin population displayed by Figure 7 clearly shows that the changes in the bonding occur in the quintet state after the transition state. At values of the IRC less than 1.0 the  $N_2O$  moiety is almost linear and therefore there is a large  $V(N1,N2)$  basin, at larger values the  $\angle ON1N2$  angle decreases and a new basin  $V(N1)$  appears, in agreement with the VSEPR prescription for a bent geometry. A fold catastrophe merges the  $V(O,N1)$  into  $V(N1)$ . All along the quintet IRC, the  $C(U) + V(U)$  population is very close to 30.0 e, which is that expected for  $U^{2+}$ . In fact, the electron density in the external core subshell is unpaired and therefore it cannot be mixed with that of the oxygen lone pairs. In the triplet state, the  $5f_{\sigma}$  orbital is doubly occupied which enables a transfer of paired density toward oxygen. Consequently, the  $C(U) + V(U)$  basin population decreases by an amount of ca. 1.4 e. The bonding in the  $UO^{2+}$  fragment is mostly ionic  $U^{4+} + O^{2-}$  with a contribution of the mesomeric structure  $U^{2+} + O$  testified by a rather large covariance of the  $C(U)$  and  $V(U,O)$  basin populations ( $\sim -1.0$ ) and by the localization of the spin density in the uranium core. In the triplet state, the  $N_2$  fragment has the characteristics of an independent closed shell molecular species.

**3.2.4. Reaction 2b Mechanism.** For this reaction, it had not been possible to localize the crossing point between the quintet



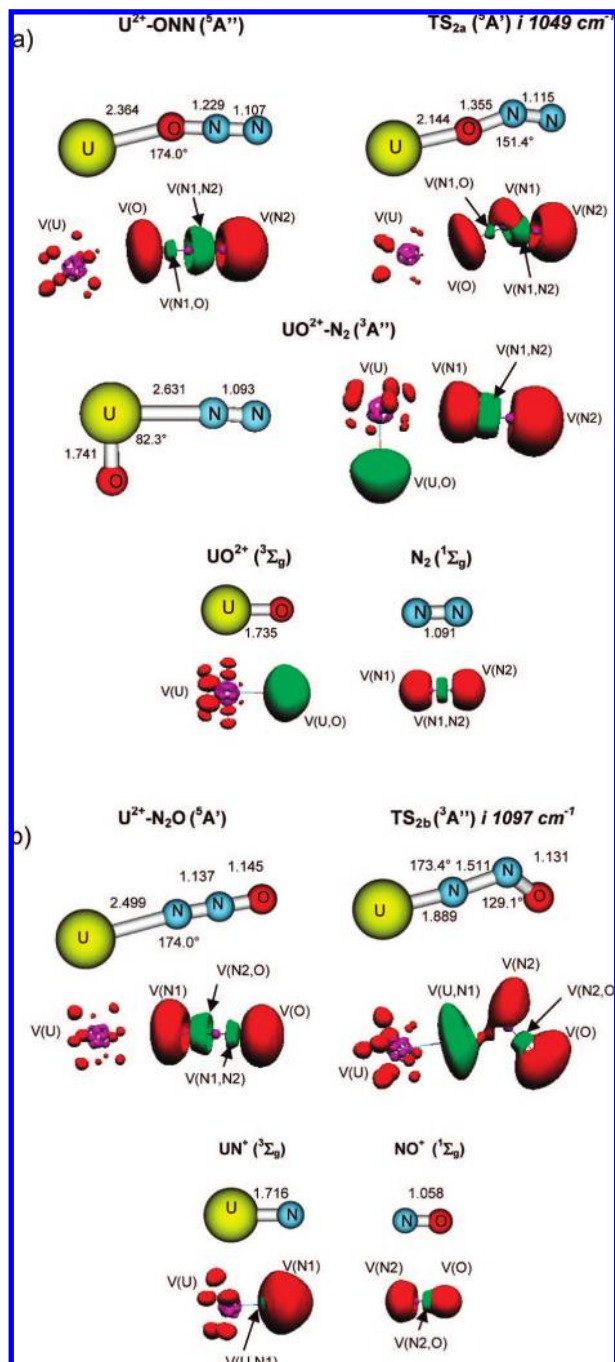


**Figure 6.** Geometrical parameters and ELF localization domains ( $\eta = 0.75$ ) of the lowest-energy minima and transition states corresponding to (a) reaction channel **2a** and (b) reaction channel **2b**. Bond lengths are in angstrom and angles in degrees.

and triplet states (Figure 8). The large energy difference between the two transition states (see Figure 5b), as well as rather large geometrical differences can be the principal reasons of this failure. However, it has been possible to follow the basin populations along a large part of both states intrinsic reaction coordinates. All the IRC points calculated for the quintet state have energies always larger than those of the triplet and therefore are helpless to discuss the mechanism. The animation (reac2b.mpeg file available in the Supporting Information) is restricted to the triplet results as well as the graph of the basin population vs IRC of Figure and 9. The quintet reactant complex appears to be the union of the  $U^{2+}$  and  $N_2O$  moieties: the spin density is localized on  $U^{2+}$  and there is no charge transfer between the

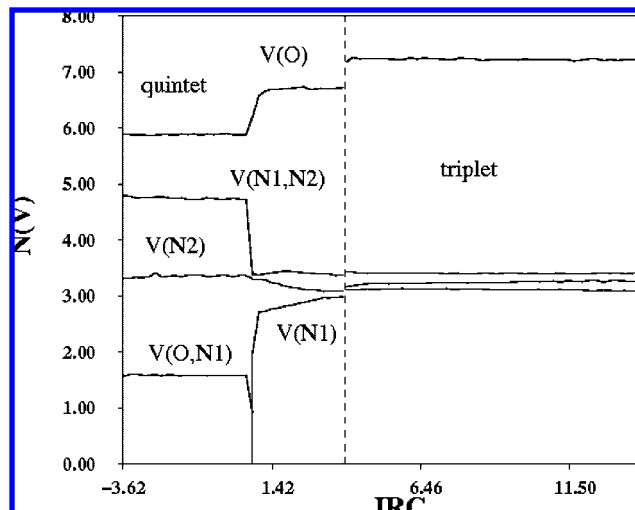


**Figure 7.** Evolution of the basin populations of the  $N_2O$  moiety along the IRC (arbitrary units) for reaction **2a**. The part on the left side of the vertical dashed line corresponds to the quintet state, on the right side to the triplet.

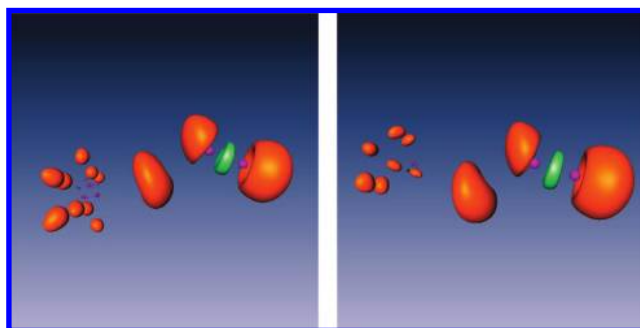


**Figure 8.** ELF localization domains ( $\eta = 0.75$ ) of the quintet (left) and of the triplet (right) in the neighborhood of the crossing point.

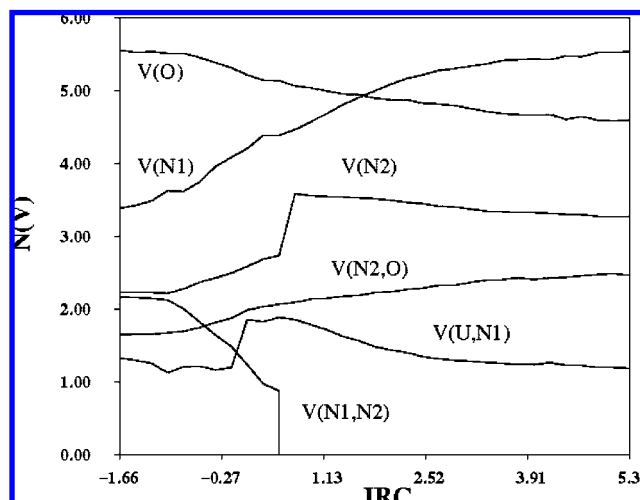


**Figure 9.** Evolution of the basin populations of the  $N_2O$  moiety along the IRC (arbitrary units) for reaction **2b** in the triplet state.

fragments. In the triplet state, the charge transfer toward  $N_2O$  is possible, accordingly the  $C(U) + V(U)$  population decreases to 29.7 and  $V(N1,N2)$  gives rise to a new basin,  $V(N2)$ , which explains the bent geometry around  $N2$ . The  $V(N1,N2)$  population consistently decreases, just before the TS a cusp catastrophe split it into two monosynaptic basins later merged into  $V(N2)$  and  $V(U,N1)$ .



#### 4. Summary and Conclusions

The main conclusions driven from the energetical analysis of the studied reactions can be summarized as follows. All the studied reactions are exothermic processes that do not involve reaction barriers over the reactants asymptotes. The main difference between the reactions of  $U^+$  and  $U^{2+}$  is that in the first case the electronic spin is conserved overall whereas in the second there are crossings between surfaces of different spin. The formation of  $UO^+ + N_2$  from the  $U^+/N_2O$  couple is the reaction with the higher exothermicity ( $-133.4$  kcal/mol) and involves the lowest intrinsic barrier height (6 kcal/mol). The formation of  $UN^+ + NO$  involves a dissociation barrier of almost 12 kcal/mol and has an exothermicity of around 14 kcal/mol. These results supports the experimental reports that indicate that the reaction is very efficient with the formation of  $UO^+$  as the primary reaction product.

According to our calculations  $U^{2+}$  reacts with  $N_2O$  to form  $UO^{2+} + N_2$  and  $UN^+ + NO^+$  in exothermic processes ( $-100$  kcal/mol for the first reaction and  $-59.8$  kcal/mol for the second). Both reactions involve crossings between the quintet and triplet spin surfaces. For the first reaction that crossing takes place after the transition state, whereas in the second the crossing occurs just before the transition state. In both cases such crossings occur at energies below the reactant asymptote.

The ELF analysis provides a clear description of the reactions between  $N_2O$  and the uranium cation and dication. In the case of  $U^+ + N_2O$ , the electronic state of the isolated cation enables a charge transfer toward  $N_2O$  the effect of which is the appearance of a monosynaptic basin on the central nitrogen center correlated with a decrease of the  $V(N1,N2)$  population and with the change from a linear to a bent geometry of the fragment. The UNN and NNO in-plane bending modes are the driving internal coordinates of the reaction. Two routes are possible from the TS: in **1a** the N–O bond is broken in a dative fashion because the  $V(N,O)$  basin becomes monosynaptic, the reaction ends with the formation of an open shell fragment  $UO^+$  and of a closed shell fragment  $N_2$ ; in reaction **1b** the covalent N–N bond is broken, giving rise to two open shell fragments. The breaking of a dative bond requires less energy than that of a covalent one, and therefore, the **1a** reaction is favored.

The complexes of  $U^{2+}$  with  $N_2O$  have both quintet ground states that prevent any charge transfer between the fragments. In the triplet state, the charge transfer is possible, provoking the same effects as in the  $U^+ + N_2O$  reactions. Two mechanisms are observed in the triplet state: on the one hand, the breaking of a dative bond yielding an open shell fragment ( $UO^{2+}$ ) and a closed shell fragment ( $N_2$ ) and, on the other hand, the breaking of a covalent bond leading to the formation of two open shell fragments ( $UN^+$  and  $NO^+$ ), this latter being energetically less favorable than the former.

**Acknowledgment.** Financial support from the Università degli Studi della Calabria is gratefully acknowledged. N.R. thanks the HPC-Europe for the grand IDRIS-62007.

**Supporting Information Available:** Three files showing an animation of the reaction pathways **1a** (reac1a.mpeg), **2a** (reac2a.mpeg) and **2b** (reac2b.mpeg). This material is available free of charge via the Internet at <http://pubs.acs.org>.

#### References and Notes

- (1) Gibson, J. K. *Int. J. Mass Spectrom.* **2002**, *214*, 1.
- (2) Gibson, J. K.; Marçalo, J. *Coord. Chem. Rev.* **2006**, *250*, 776.
- (3) Cornehl, H. H.; Heinemann, C.; Marçalo, J.; Pires de Matos, A.; Schwarz, H. *Angew. Chem., Int. Ed. Engl.* **1996**, *35*, 891.
- (4) Cornehl, H. H.; Wesendrup, R.; Diefenbach, M.; Schwarz, H. *Chem. Eur. J.* **1997**, *3*, 1083.
- (5) Santos, M.; Marçalo, J.; Pires de Matos, A.; Gibson, J. K.; Haire, R. G. *J. Phys. Chem. A* **2002**, *106*, 7190.
- (6) Santos, M.; Marçalo, J.; Leal, J. P.; Pires de Matos, A.; Gibson, J. K.; Haire, R. G. *Int. J. Mass Spectrom.* **2003**, *228*, 457.
- (7) Gibson, J. K.; Haire, R. G.; Santos, M.; Marçalo, J.; Pires de Matos, A. *J. Phys. Chem. A* **2005**, *109*, 2768.
- (8) Michelini, M. C.; Russo, N.; Sicilia, E. *Angew. Chem., Int. Ed.* **2006**, *45*, 1095.
- (9) Michelini, M. C.; Russo, N.; Sicilia, E. *J. Am. Chem. Soc.* **2007**, *129*, 4229.
- (10) Mazzzone, G.; Michelini, M. C.; Russo, N.; Sicilia, E. *Inorg. Chem.* **2008**, *47*, 2083.
- (11) (a) Armentrout, P. B.; Beauchamp, J. L. *Acc. Chem. Res.* **1989**, *22*, 315. (b) Schröder, D.; Shaik, S.; Schwarz, H. *Acc. Chem. Res.* **2000**, *33*, 139. (c) Poli, R.; Harvey, J. N. *Chem. Soc. Rev.* **2003**, *32*, 1.
- (12) See for instance: (a) Yarkony, D. R. *Int. Rev. Phys. Chem.* **1992**, *11*, 195. (b) Yarkony, D. R. *J. Phys. Chem.* **1996**, *100*, 18612. (c) Irigoras, A.; Fowler, J. E.; Ugalde, J. M. *J. Phys. Chem. A* **1998**, *102*, 293. (d) Irigoras, A.; Fowler, J. E.; Ugalde, J. M. *J. Am. Chem. Soc.* **1999**, *121*, 574. (e) Irigoras, A.; Fowler, J. E.; Ugalde, J. M. *J. Am. Chem. Soc.* **1999**, *121*, 8549. (f) Irigoras, A.; Elizalde, O.; Silanes, I.; Fowler, J. E.; Ugalde, J. M. *J. Am. Chem. Soc.* **2000**, *122*, 114. (g) Michelini, M. C.; Russo, N.; Sicilia, E. *J. Phys. Chem. A* **2002**, *106*, 8937. (h) Chiodo, S.; Kondakova, O.; Michelini, M. C.; Russo, N.; Sicilia, E. *Inorg. Chem.* **2003**, *42*, 8773. (i) Harvey, J. N.; Poli, R.; Smith, K. M. *Coord. Chem. Rev.* **2003**, *238/239*, 347. (j) Shaik, S.; Cohen, S.; de Visser, S. P.; Sharma, P. K.; Kumar, D.; Kozuch, S.; Ogliaro, F.; Danovich, D. *Eur. J. Inorg. Chem.* **2004**, *35*, 207. (k) Schwarz, H. *Int. J. Mass Spectrom.* **2004**, *237*, 75. (l) Chiodo, S.; Kondakova, O.; Michelini, M. C.; Russo, N.; Sicilia, E. *J. Phys. Chem. A* **2004**, *108*, 10–69. (m) Michelini, M. C.; Russo, N.; Alikhani, M. E.; Silvi, B. *J. Comput. Chem.* **2004**, *25*, 1647. (n) Michelini, M. C.; Russo, N.; Sicilia, E. *Inorg. Chem.* **2004**, *43*, 4944. (o) Mercero, J. M.; Matxain, J. M.; Lopez, X.; York, D. M.; Largo, A.; Eriksson, L. A.; Ugalde, J. M. *Int. J. Mass Spectrom.* **2005**, *240*, 37. (p) Martinez, M.; Rivalta, I.; Michelini, M. C.; Russo, N.; Sicilia, E. *Inorg. Chem.* **2005**, *44*, 9807.
- (13) (a) Gagliardi, L.; La Manna, G.; Roos, B. O. *Faraday Discuss.* **2003**, *124*, 63. (b) Balasubramanian, K.; Siekhaus, W. J.; McLean, W., II. *J. Chem. Phys.* **2003**, *119*, 5889.
- (14) (a) Liang, B.; Andrews, L.; Li, J.; Bursten, B. E. *J. Am. Chem. Soc.* **2002**, *124*, 6723. (b) Andrews, L.; Kushto, G. P.; Marsden, C. J. *Chem. Eur. J.* **2006**, *12*, 8324. (c) Wang, X.; Andrews, L.; Marsden, C. J. *Chem. Eur. J.* **2007**, *13*, 5601.
- (15) (a) Lavrov, V. V.; Blagojevic, V.; Koyanagi, G. K.; Orlova, G.; Bohme, D. K. *J. Phys. Chem. A* **2004**, *108*, 5610. (b) Bohme, D. K.; Schwarz, H. *Angew. Chem., Int. Ed.* **2005**, *44*, 2336. (c) Blagojevic, V.; Orlova, G.; Bohme, D. K. *J. Am. Chem. Soc.* **2005**, *127*, 3545.
- (16) Koyanagi, G. K.; Bohme, D. K. *J. Phys. Chem. A* **2001**, *105*, 8964.
- (17) See for instance (a) Delabie, A.; Vinckier, C.; Flock, M.; Pierloot, K. *J. Phys. Chem. A* **2001**, *105*, 5479. (b) Delabie, A.; Pierloot, K. *J. Phys. Chem. A* **2002**, *106*, 5679. (c) Yang, X.-Y.; Wang, Y.-C.; Geng, Z. Y.; Liu, Z.-Y. *Chem. Phys. Lett.* **2006**, *430*, 265.
- (18) (a) Becke, A. D. *J. Chem. Phys.* **1993**, *98*, 5648. (b) Lee, C.; Yang, W.; Parr, R. G. *Phys. Rev. B* **1988**, *37*, 785.
- (19) (a) <http://www.theochem.unistuttgart.de/pseudopotentiale/>. (b) Küchle, W.; Dolg, M.; Stoll, H.; Preuss, H. *J. Chem. Phys.* **1994**, *100*, 7535.
- (20) (a) Krishnan, R.; Binkley, J. S.; Seeger, R.; Pople, J. A. *J. Chem. Phys.* **1980**, *72*, 650. (b) Blaudau, J.-P.; McGrath, M. P.; Curtiss, L. A.; Radom, L. *J. Chem. Phys.* **1997**, *107*, 5016. (c) Clark, T.; Chandrasekhar, J.; Schleyer, P. v. R. *J. Comput. Chem.* **1983**, *4*, 294.
- (21) Frisch, M. J.; Trucks, G. W.; Schlegel, H. B.; Scuseria, G. E.; Robb, M. A.; Cheeseman, J. R.; Montgomery, J. A., Jr.; Vreven, T.; Kudin, K. N.; Burant, J. C.; Millam, J. M.; Iyengar, S. S.; Tomasi, J.; Barone, V.; Mennucci, B.; Cossi, M.; Scalmani, G.; Rega, N.; Petersson, G. A.; Nakatsuji, H.; Hada, M.; Ehara, M.; Toyota, K.; Fukuda, R.; Hasegawa, J.; Ishida, M.; Nakajima, T.; Honda, Y.; Kitao, O.; Nakai, H.; Klene, M.; Li, X.; Knox, J. E.; Hratchian, H. P.; Cross, J. B.; Bakken, V.; Adamo, C.; Jaramillo, J.; Gomperts, R.; Stratmann, R. E.; Yazyev, O.; Austin, A. J.; Cammi, R.; Pomelli, C.; Ochterski, J. W.; Ayala, P. Y.; Morokuma, K.; Voth, G. A.; Salvador, P.; Dannenberg, J. J.; Zakrzewski, V. G.; Dapprich, S.; Daniels, A. D.; Strain, M. C.; Farkas, O.; Malick, D. K.; Rabuck, A. D.; Raghavachari, K.; Foresman, J. B.; Ortiz, J. V.; Cui, Q.; Baboul, A. G.; Clifford, S.; Cioslowski, J.; Stefanov, B. B.; Liu, G.; Liashenko, A.; Piskorz, P.; Komaromi, I.; Martin, R. L.; Fox, D. J.; Keith, T.; Al-Laham, M. A.; Peng, C. Y.; Nanayakkara, A.; Challacombe, M.; Gill, P. M. W.; Johnson, B.; Chen, W.; Wong, M. W.; Gonzalez, C.; Pople, J. A. *Gaussian 03*, revision C.02; Gaussian, Inc.: Wallingford, CT, 2004.
- (22) (a) Noury, S.; Krokidis, X.; Fuster, F.; Silvi, B. *TopMod Package*; Paris, 1997. (b) Noury, S.; Krokidis, X.; Fuster, F.; Silvi, B. *Comput. Chem.* **1999**, *23*, 597.

- (23) Flükiger, P.; Lüthi, H.-P.; Portmann, S.; Weber, J. *MOLEKEL 4.0*; Swiss National Supercomputing Centre CSCS, Manno (Switzerland), 2000.
- (24) *Amira 3.0*; TGS, Template Graphics Software, Inc.: San Diego, 2002.
- (25) Silvi, B.; Savin, A. *Nature* **1994**, *371*, 683.
- (26) Becke, A. D.; Edgecombe, K. E. *J. Chem. Phys.* **1990**, *92*, 5397.
- (27) Gillespie, R. J.; Robinson, E. A. *J. Comput. Chem.* **2007**, *28*, 87.
- (28) Silvi, B. *Phys. Chem. Chem. Phys.* **2004**, *6*, 256.
- (29) Silvi, B.; Fourré, I.; Alikhani, M. E. *Monatsh. Chem.* **2005**, *136*, 855.
- (30) Krokidis, X.; Noury, S.; Silvi, B. *J. Phys. Chem. A* **1997**, *101*, 7277.
- (31) Thom, R. *Stabilité Structurale et Morphogénèse*; Interdictions: Paris, 1972.
- (32) See for instance: (a) Krokidis, X.; Silvi, B.; Alikhani, M. E. *Chem. Phys. Lett.* **1998**, *292*, 35. (b) Krokidis, X.; Silvi, B.; Cezarnaud-Dandine, C.; Sevin, A. *New. J. Chem.* **1998**, *22*, 1341. (c) Berski, S.; Andrés, J.; Silvi, B.; Domingo, L. R. *J. Phys. Chem. A* **2003**, *107*, 6014. (d) Polo, V.; Andrés, J.; Castillo, R.; Berski, S.; Silvi, B. *Chem. Eur. J.* **2004**, *10*, 5165.
- (e) Santos, J. C.; Polo, V.; Andrés, J. *Chem. Phys. Lett.* **2005**, *406*, 393. (f) Berski, S.; Andrés, J.; Silvi, B.; Domingo, L. R. *J. Phys. Chem. A* **2006**, *110*, 13939.
- (33) Blaise, J.; Wyart, J.-F. International Tables of Selected Constants, Energy Levels and Atomic spectra of Actinides, Vol. 20, Tables of Constants and Numerical Data, Paris, 1992, taken from <http://www.lac.u-psud.fr/Database/Contents.html>.
- (34) Lias, S. G.; Bartmess, J. E.; Liebman, J. F.; Holmes, J. L.; Levin, R. D.; Mallard, W. G. *J. Phys. Chem. Ref. Data* **1988**, *17* (Suppl. 1).
- (35) Michelini, M. C.; Russo, N.; Alikhani, M. E.; Silvi, B. *J. Comput. Chem.* **2005**, *26*, 1284.
- (36) Llusar, R.; Beltrán, A.; Andrés, J.; Noury, S.; Silvi, B. *J. Comput. Chem.* **1999**, *20*, 1517.
- (37) Morss, L. R. In *The Chemistry of the Actinide Elements*, 2nd ed.; Katz, J. J., Seaborg, G. T., Morss, L. R., Eds.; London: Chapman & Hall, 1986; Vol. 2.

JP803269J